

Cite this: *J. Mater. Chem. B*, 2023, **11**, 11578

Ultrasmall calcium-enriched Prussian blue nanozymes promote chronic wound healing by remodeling the wound microenvironment†

Qingrong Dong,^{abc} Ge Fang,^{ib}*^b Fang Liu,^{bd} Shuwei Cai,^b Yujie Tao,^b Tingyu Xue,^{abc} Minghua Tang,^e Kun Zhang,^d Ziheng An,^b Jiangfeng Du^{ib}*^{acd} and Hui Zhang*^{ac}

Chronic wound healing remains challenging due to the oxidative microenvironment. Prussian blue (PB) nanoparticles exhibiting multiple antioxidant enzyme-like activities have attracted widespread attention, while their antioxidant efficacy remains unsatisfied. Herein, ultrasmall calcium-enriched Prussian blue nanoparticles (CaPB NPs) are simply constructed with high yields for the wound repair application. Owing to the ultrasmall size and synergistic effect of the generated dual active sites, the CaPB NPs exhibit prominent antioxidant-like activities, protecting cells from oxidative stress-induced damage. In addition to the effect of Ca on regulating keratinocyte and fibroblast growth, it has been demonstrated that the administration of CaPB NPs obviously promoted wound closure as well as collagen deposition and neovascularization in the full-thickness wound defect model in mice. Importantly, the CaPB NP treatment can effectively up-regulate the expression levels of anti-inflammatory cytokines and vascular endothelial growth factors to remodel the wound microenvironment, thereby accelerating the wound healing process. Overall, this work reveals that metal atom substitution is an effective strategy to construct ultrasmall and high-catalytic-performance PB-based nanozymes and further potentiate their effectiveness for chronic wound management.

Received 5th September 2023,
Accepted 15th November 2023

DOI: 10.1039/d3tb02065g

rsc.li/materials-b

Introduction

Chronic, non-healing wounds represent a substantial financial burden on healthcare systems and communities.¹ It has been estimated that there are more than 6.5 million patients with chronic wounds globally and treating those wounds annually costs more than 25 million US dollars.^{2,3} Therefore, it is crucial to explore novel strategies that promote wound healing. Although the definite mechanisms of poor wound healing are not yet well-understood, impaired wound healing has been mainly attributed to excessive reactive oxygen species and

untreated inflammations, which disrupt the cellular antioxidant system and impede the healing process.^{4–6}

Traditionally, addition of natural antioxidants including antioxidant enzymes^{7,8} (such as superoxide dismutase (SOD), catalase (CAT), glutathione peroxidase, *etc.*) and nonenzymatic antioxidants (such as vitamin C, nitric oxide, metal-binding proteins, *etc.*) can effectively scavenge reactive oxygen species (ROS), increase angiogenesis, reduce inflammatory response, and stimulate fibroblast and keratinocyte proliferation. However, their clinical applications are hindered by low stability, the need for particular protective conditions to preserve their intrinsic activity, and their inability to replenish sufficiently during long disease progression.^{9–11} Therefore, novel drugs or strategies with high antioxidant/anti-inflammatory capacity are still urgently needed for rapid and successful chronic wound repair.

Recently, nanozymes have attracted increasing attention owing to their outstanding features such as their inherent enzymatic activity, high stability and low cost.^{12,13} Currently, a large number of nanomaterials including carbon, noble metals, and metal oxides have been discovered to mimic antioxidant enzyme-like activities.^{14,15} Among them, Prussian blue (PB) nanoparticles, consisting of divalent iron ions connected by a cyanide bridge, have gained attention with multienzyme-like activities and the U.S.

^a Department of Medical Imaging, First Hospital of Shanxi Medical University, Taiyuan 030001, China. E-mail: dujf@sxmu.edu.cn, zhang_hui@sxmu.edu.cn

^b State Key Laboratory of Radiation Medicine and Protection, School of Radiation Medicine and Protection, School for Radiological and Interdisciplinary Sciences (RAD-X), Collaborative Innovation Center of Radiation Medicine of Jiangsu Higher Education Institutions, Soochow University, Suzhou 215123, China. E-mail: gfang@suda.edu.cn

^c Intelligent Imaging Big Data and Functional Nano-imaging Engineering Research Center of Shanxi Province, Taiyuan 030001, China

^d College of Pharmacy, Shanxi Medical University, Jinzhong 030619, China

^e Analysis and Testing Center, Soochow University, Suzhou 215123, China

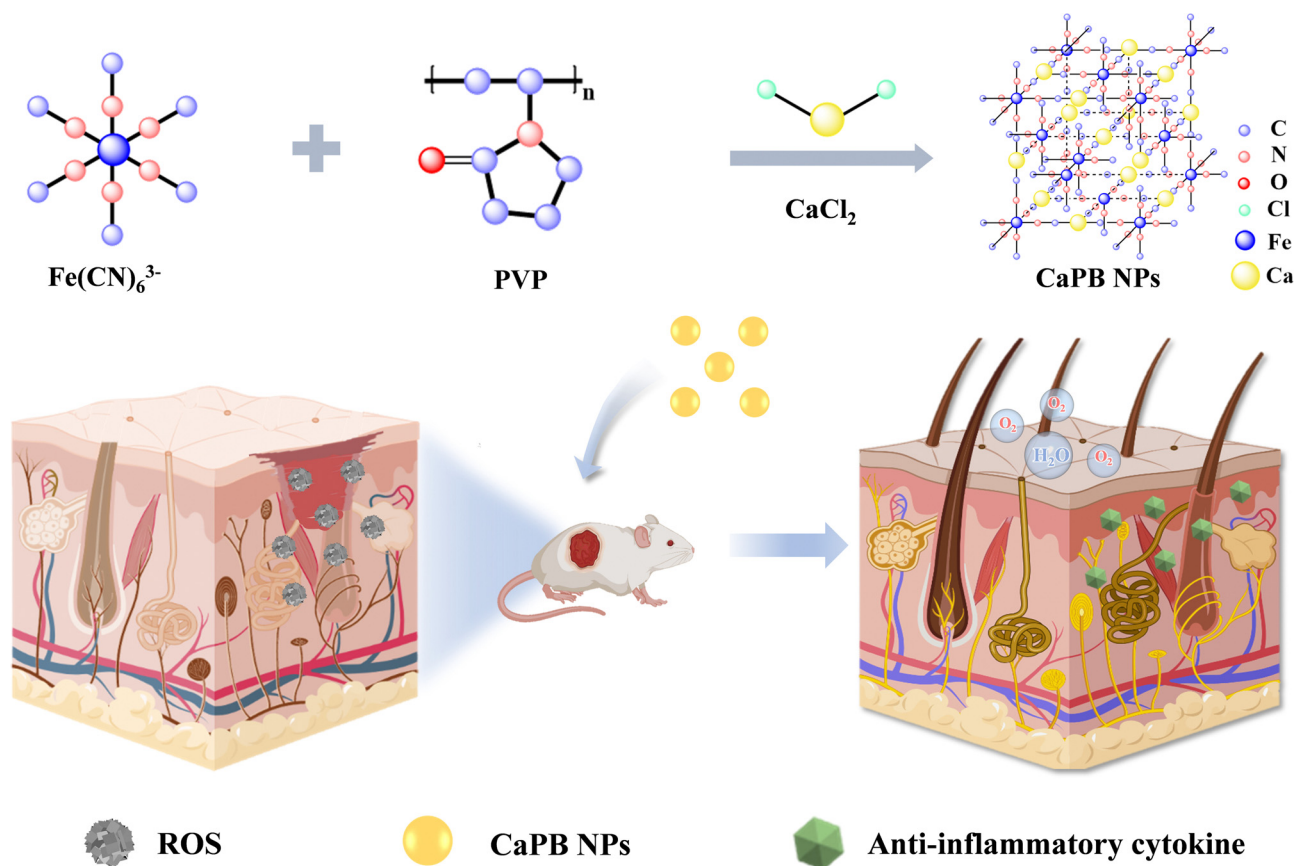
† Electronic supplementary information (ESI) available. See DOI: <https://doi.org/10.1039/d3tb02065g>

Food and Drug Administration-approved biosafety.¹⁶ Especially, PB has been extensively studied in the field of wound healing owing to its potent antioxidant activity and anti-inflammatory properties.^{17–19} For instance, Sahu *et al.*²⁰ have demonstrated that Prussian blue nanozymes could accelerate the healing process in a wound model through mitigating excessive ROS and modulating inflammation. The group of Wu²¹ developed a composite nanofiber containing PB and heparin sodium (Hep) for repairing diabetic wounds. The integrated nanofibers exerted a synergistic treatment effect owing to the excellent pro-inflammatory factor-adsorbing capability of Hep and the ROS-scavenging capabilities of PB. Despite the great potential of PB in wound healing, the practical applications have been hindered by its unsatisfied enzymatic activity. In general, size is a key factor to modulate the enzyme-like activity of nanozymes.²² However, size-controllable synthesis and mass production of ultrasmall PB NPs (USPBs) remain challenging owing to their low solubility and high formation speed.²³ Therefore, it is of great significance to improve their antioxidant enzyme-like activities through the synthesis of small sized particles.

Previous studies have revealed that constructing Prussian blue analogues (PBAs) is an effective strategy for achieving small-size and large-scale synthesis of USPBs

and meanwhile exhibiting considerable catalytic activity owing to the synergistic effect of dual active sites $M_x(CN)_y$. For example, Wang *et al.* constructed Gd-PBAs, which increased the CAT-like activity by over 4 times compared with pristine PB NPs. Mechanism analysis revealed that the induction of gadolinium successfully regulated the oxidation state of Fe to more easily exert antioxidant activity and meanwhile reduced the Gibbs free energy of the catalytic reaction, thus accelerating the catalytic process.²⁴ In addition, a series of studies have demonstrated the functions and roles of Ca in skin regeneration and reconstruction through modulating proliferation, differentiation, and maturation of keratinocytes and fibroblasts, as well as the formation of the epidermal lipid barrier function during wound healing.^{25,26}

Therefore, in this study, ultrasmall Ca-enriched PB nanoparticles were rationally designed and employed as antioxidant enzyme mimics to promote chronic wound healing. CaPB NPs have excellent CAT-like and SOD-like activities and could protect cells against oxidative damage. Importantly, *in vivo* experiments have demonstrated that CaPB NPs were able to promote the wound healing through scavenging the ROS and modulating the inflammation microenvironment in the wound site (Scheme 1). It is highly expected that CaPB



Scheme 1 Schematic illustration of CaPB NPs for the treatment of chronic wounds.

NPs could facilitate the development of multifunctional nanozymes and open a new avenue for the treatment of chronic wound healing.

Results and discussion

Synthesis and characterization of CaPB NPs

The CaPB NPs were synthesized by a convenient polymer-instructed nucleation process (Fig. 1a) according to previous literature.²⁷ The as-synthesized product presented a spherical

morphology with an average size of 4.92 nm by transmission electron microscopy (Fig. 1b). Also, through the dynamic light scattering method, the hydrodynamic diameters of the CaPB NPs were determined to be 8.17 ± 2.28 nm (Fig. 1c). Furthermore, the energy dispersive X-ray spectroscopy (EDX) measurements presented the uniform distribution of corresponding elements including Ca and Fe, confirming the successful doping of Ca (Fig. S1 and S2, ESI[†]). Fourier transform infrared spectroscopy (FTIR) showed the characteristic peaks of $-\text{C}\equiv\text{N}$ - and $\text{C}=\text{O}$, revealing the presence of the metallic cyanide

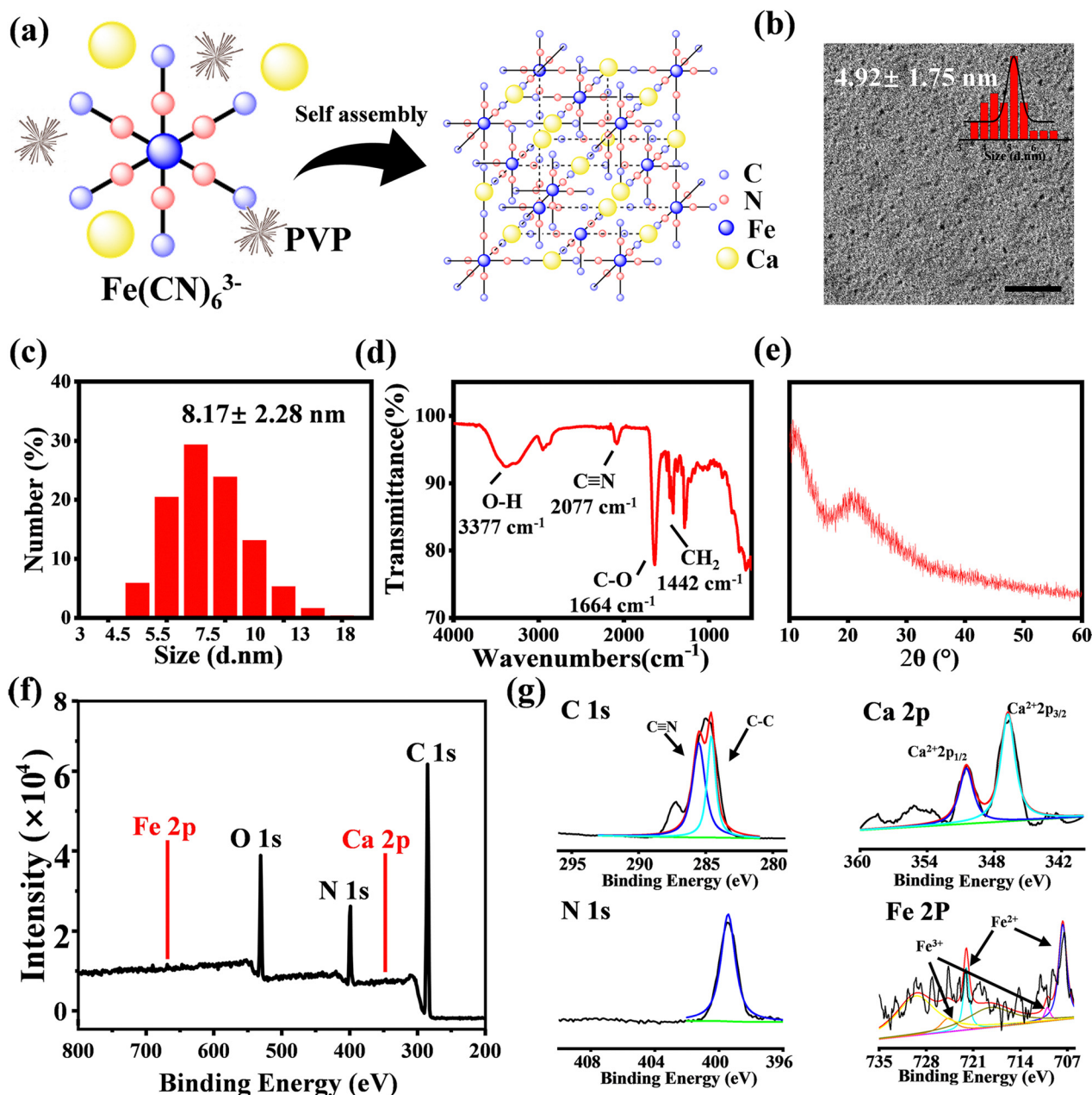


Fig. 1 Synthesis and characterization of CaPB NPs. (a) Illustration of Ca^{2+} -doped Prussian blue frameworks. (b) TEM image of CaPB NPs. The scale bar represents 50 nm. The inset presents the corresponding size distribution of CaPB NPs analyzed using Nano measure software. (c) Size distribution of CaPB NPs. (d) FT-IR spectrum of CaPB NPs. (e) XRD spectra of CaPB NPs. (f) XPS spectrum of CaPB NPs and the corresponding high-resolution spectra of C1s, N1s, Fe2p, and Ca2p.

structure and PVP, respectively (Fig. 1d). The characteristic peaks of the PVP polymer were found in the X-ray diffraction (XRD) pattern of CaPB NPs (Fig. 1e). The X-ray photoelectron spectroscopy (XPS) spectra also implied the coexistence of Ca, Fe, C, N, and O (Fig. 1f). Consistently, the high-resolution XPS spectrum showed that the C1s peak could be divided into C–C bonding (284.8 eV), C–N bonding (285.7 eV), C–O bonding (286.8 eV) and C=O bonding (288.8 eV), further revealing the presence of PVP. The N1s spectrum could be deconvoluted into C–N bonding (400.4 eV) and C≡N bonding (398.9 eV), which was attributable to the cyanogen groups of CaPB NPs. According to the Fe2p and Ca2p spectra (Fig. 1g), the presence of multivalent iron and Ca^{II} species was confirmed. These above results show that CaPB NPs were successfully prepared.

ROS scavenging activity of CaPB NPs

Hydrogen peroxide (H₂O₂) and superoxide oxygen anions O₂^{•-} have been considered as the most abundant ROS species generated in cells in the process of wound injury. CAT and SOD, as the main antioxidant enzymes, are responsible for the degradation of H₂O₂ and elimination of O₂^{•-}, respectively. Therefore, multiple antioxidant enzyme-like activities of CaPB NPs were evaluated *via* model reactions and for comparison, ultrasmall PB NPs (USPBs) with similar sizes were synthesized (Fig. S4 and S5, ESI†).²³ First, the CAT-like activity of CaPB NPs was determined by monitoring the decrease of the H₂O₂ concentration using a H₂O₂ detection assay (Beyotime, China). In the presence of CaPB NPs, there was a significant decrease of the remaining H₂O₂ as the concentration of CaPB NPs, indicating that the CaPB NPs could exhibit CAT-mimicking activity

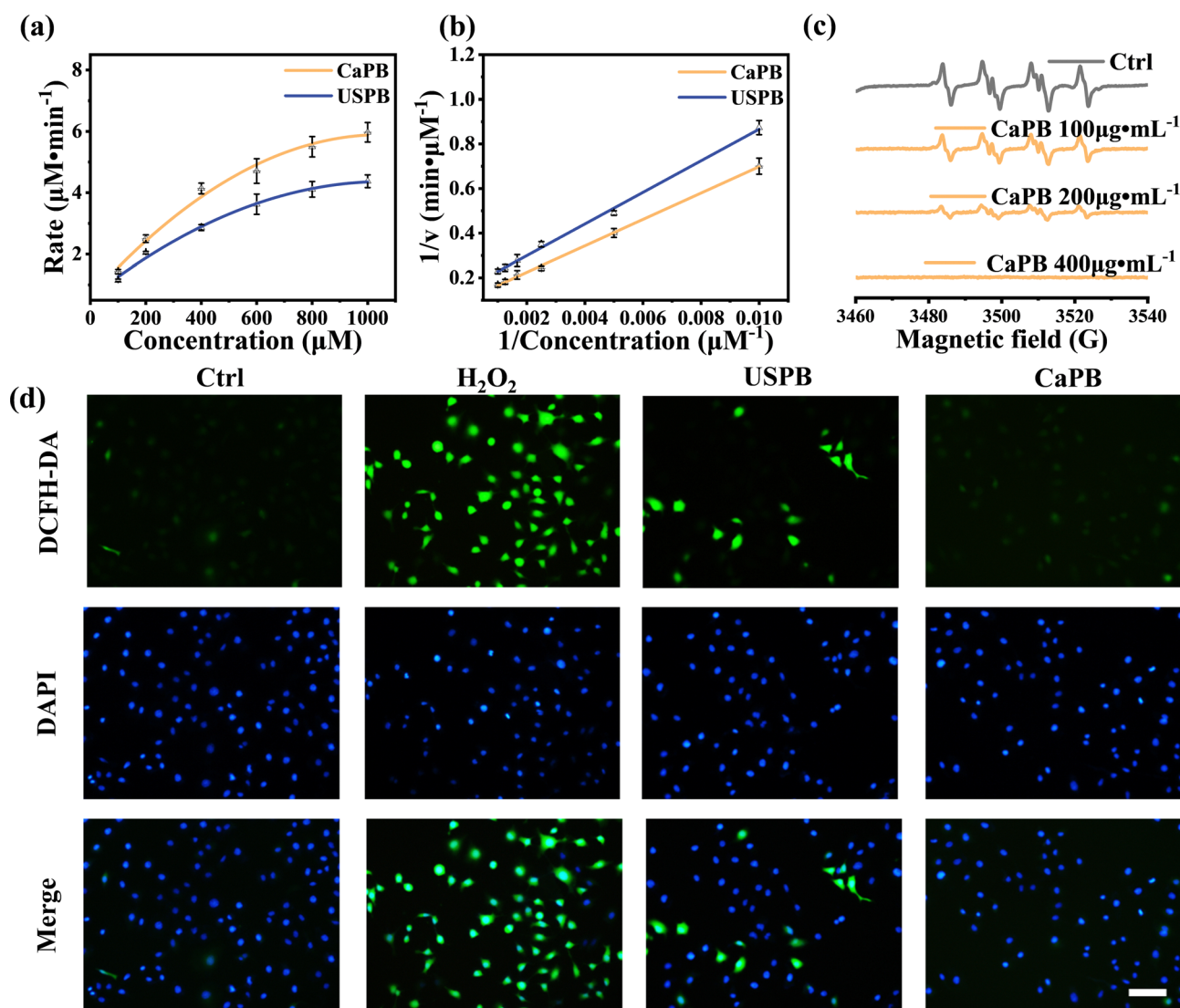


Fig. 2 Antioxidant performance of CaPB NPs. (a) Michaelis–Menten kinetic analysis of CaPB NPs and USPBs. (b) Double-reciprocal plots for determining the kinetic parameters of CaPB NPs and USPBs. (c) ESR spectra for determining the SOD-like activity. (d) Fluorescence images of HUVEC cells after different treatments stained with DCFH-DA and DAPI. The scale bar represents 50 μm.

Table 1 Comparison of the kinetic parameters of CaPB NPs and USPBs

Materials	[S] (μM)	K_m ($\times 10^2 \mu\text{M}$)	V_{max} ($\mu\text{M min}^{-1}$)	K_{cat} (10^{-2}min^{-1})	K_{cat}/K_m ($\times 10^{-4} \mu\text{M}^{-1} \text{min}^{-1}$)
CaPB NPs	100	5.55	9.38	9.38	1.69
USPB NPs	100	4.5	8.33	8.33	1.85

(Fig. S6, ESI[†]). The steady-state kinetic analysis was conducted at various concentrations of H_2O_2 . By plotting the initial reaction velocities against the H_2O_2 concentration, typical Michaelis–Menten-type saturation kinetic curves were observed (Fig. 2a). Furthermore, through the corresponding double-reciprocal plots of initial reaction rates (Fig. 2b), the apparent Michaelis–Menten constant (K_m) and maximal reaction velocity (V_{max}) were obtained to be $555 \mu\text{M}$ and $9.38 \mu\text{M min}^{-1}$, respectively. A comparison of the CAT-like activity of CaPB NPs and USPBs is presented in Table 1. Encouragingly, the CaPB NPs had a 1.13-fold higher maximum reaction rate (V_{max}) with H_2O_2 as the substrate, although the CaPB NPs had a lower affinity that is observed for USPBs.

Next, the SOD-like activity of CaPB NPs was evaluated using electron spin resonance (ESR) spectroscopy. The xanthine/xanthine oxidase system and 5-*tert*-butoxycarbonyl 5-methyl-1-pyrroline *N*-oxide (BMPO) were employed as the $\text{O}_2^{\bullet-}$ generator and the trapping agent, respectively. As shown in Fig. 2c, the ESR signal of BMPO/ $\text{O}_2^{\bullet-}$ decreased dramatically in the presence of CaPB NPs and the elimination efficiency of $\text{O}_2^{\bullet-}$ was dependent on the concentration, especially almost 100% elimination at a CaPB NP concentration of $400 \mu\text{g mL}^{-1}$. The SOD-like activity of CaPB NPs was also assessed by employing a superoxide assay kit (Beyotime, China), which revealed that the CaPB NPs also exhibited strong $\text{O}_2^{\bullet-}$ elimination ability in a concentration-dependent manner, agreeing with the results of the ESR method (Fig. S7, ESI[†]). Meanwhile, the SOD-like activity of USPBs was also confirmed by ESR (Fig. S8, ESI[†]) and compared with CaPB NPs through the SOD kit at the same iron concentration ($20 \mu\text{g mL}^{-1}$) (Fig. S9, ESI[†]), which showed that the CaPB NPs displayed slightly higher activity than that of USPBs as SOD mimics. These above results demonstrated that the CaPB NPs exhibited efficient ROS scavenging activity, which hold great potential for accelerating the wound healing. Furthermore, we have attempted to explore the modulation effect of Ca^{2+} in the enzymatic activity. Electrochemical impedance spectroscopy (EIS) analysis was performed to explore the electron transfer ability of materials.²⁸ As demonstrated by EIS, the CaPB NPs displayed lower electrochemical impedance compared with USPBs as evidenced by a slightly smaller arc radius (Fig. S10, ESI[†]), indicating that doping Ca^{2+} can promote electron transfer during the enzymatic reaction process, thereby improving the catalytic efficiency.

Encouraged by the prominent activity of CaPB NPs as CAT and SOD mimics, we explored the cytoprotective effect of CaPB NPs *in vitro*. First, no obvious cytotoxicity of CaPB NPs was observed when incubated with CaPB NPs, even in the presence of CaPB NPs up to 1.6mg mL^{-1} (Fig. S11 and S12, ESI[†]). As shown in Fig. S13 (ESI[†]), the cell viability was $41.0 \pm 1.9\%$ after treating with $1 \text{mM H}_2\text{O}_2$, which was used to simulate the

oxidative stress environment. In comparison, the cell viability improved remarkably to $84.5 \pm 2.7\%$ and $76.3 \pm 2.5\%$ with the addition of CaPB NPs and USPBs, respectively. This indicated that CaPB NPs displayed the sufficient cytoprotective effect against oxidative stress.

To confirm that the cytoprotective effect of CaPB NPs was due to the reduction in oxidative stress through their ROS scavenging ability, we used 2',7'-dichlorodihydrofluorescein diacetate (DCFH-DA) as a fluorescent probe to detect the intracellular ROS level. The strong fluorescence signal in Fig. 2d demonstrates that the ROS level in H_2O_2 -treated HUVEC cells was significantly higher than the untreated cells. However, when $400 \mu\text{g mL}^{-1}$ of CaPB NPs were added, the intracellular ROS production in H_2O_2 -stimulated cells was considerably suppressed, as shown by much weaker fluorescence signals. Quantitative analysis revealed that 80% of the ROS in H_2O_2 -stimulated cells could be scavenged by USPBs compared to 94% ROS scavenged by CaPB NPs (Fig. S14, ESI[†]). This is consistent with the earlier observation that CaPB NPs display prominent enzyme-like and antioxidant activities.

In vivo cutaneous wound healing

Based on their outstanding antioxidant activity *in vitro*, CaPB NPs have the potential to promote wound healing. Thus, we tested the therapeutic efficiency of CaPB NPs using a full-thickness wound model. First, a full-thickness wound model (10 mm) in Balb/c mice was established with a surgical scissor. Afterwards, the CaPB NPs were employed on the wound site and the healing status of the wound was monitored (Fig. 3a). The size of the wounds was measured and the wound areas were photographed daily, respectively. The representative photographs of the wounds are displayed in Fig. 3b. The wounds in each group showed an inflammatory state on the 1st day, indicating that the inflammatory wound had been successfully constructed. On the 3rd day, the wounds of the control group showed a suppurating state, while the wounds of the CaPB NP-treated group had begun to scab. Notably, on the 13th day, the CaPB NP-treated wound had completely healed, while there was still a large amount of scab formation in the untreated group. Moreover, the quantitative analysis of the wound area showed that there was a statistical difference in the closure ratio of the wound between the CaPB NP-treated and control groups ($P < 0.05$). In detail, on day 4, the closure ratio of the wound in the CaPB NP-treated group was up to $32.6 \pm 6.0\%$, while that in the control group was only $13.1 \pm 2.5\%$ (Fig. 3c). Especially, it had achieved 50% healing in the CaPB NP-treated group on day 7, while the control group needs 11 days to achieve the same healing rate. Excitingly, the wound after treatment with CaPB NPs had achieved complete healing within 13 d, while they achieved only $61.8 \pm 1.1\%$ of wound

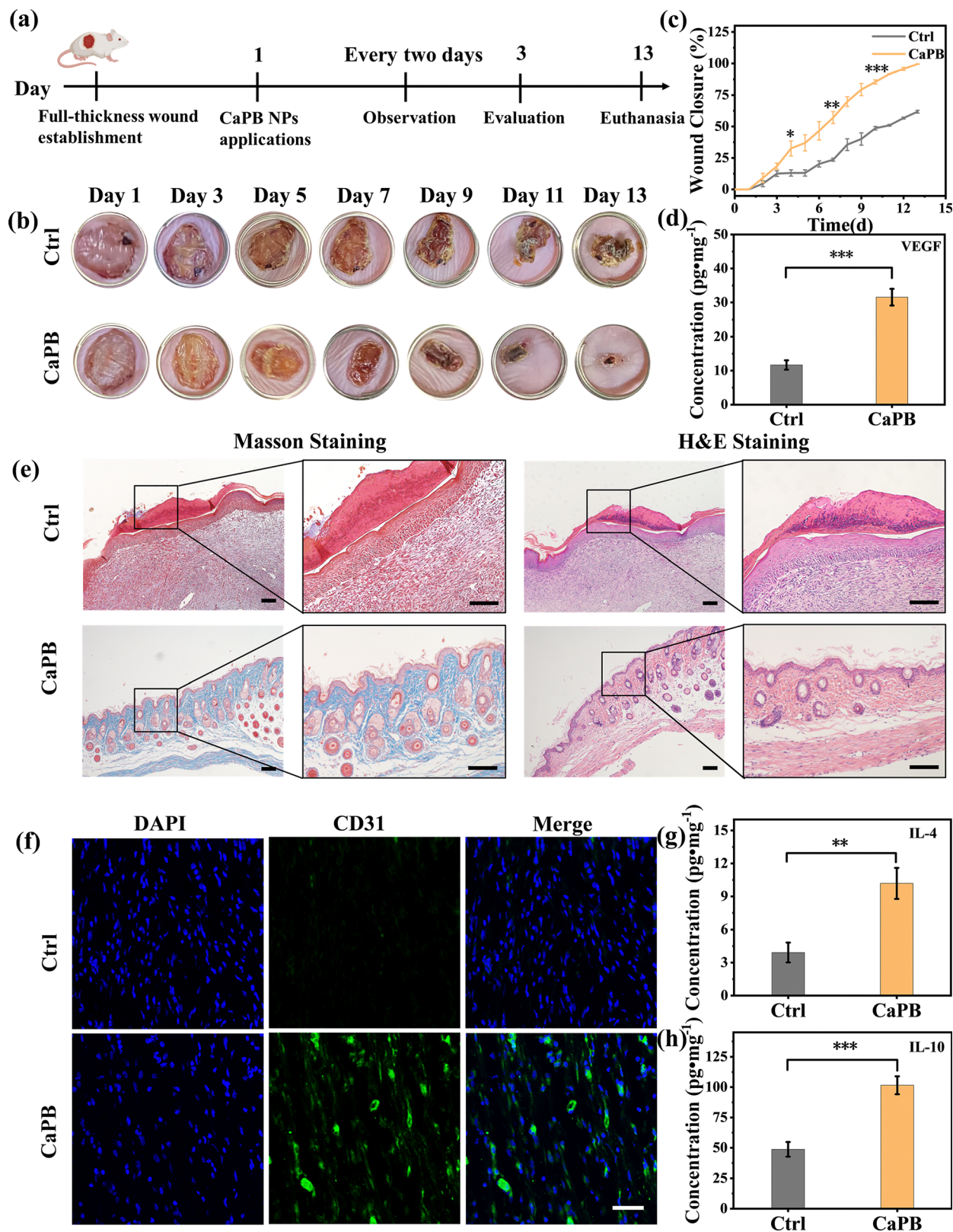


Fig. 3 (a) Experimental scheme for the CaPB NP-enabled treatment strategy in wound mice. (b) Photographs of the wound with different treatments. (c) Quantitative analysis of the wound closure rate after different treatments ($n = 3$, data represent means \pm SD, $*p < 0.05$, $**p < 0.01$, $***p < 0.001$). (e) Masson staining and H&E staining images of the collected wound tissues in different groups. The scale bar represents 100 μm . (f) Representative confocal images of immunofluorescence staining of CD31. The scale bar represents 50 μm . The expression levels of (d) VEGF, (g) IL-4, and (h) IL-10 in wound tissue homogenates with different groups ($n = 3$, data are shown as mean \pm SD, $*p < 0.05$, $**p < 0.01$, $***p < 0.001$).

closure in the control group. Meanwhile, the effect of USPBs on wound healing was also evaluated and the results showed that the promotion effect on wound healing induced by CaPB NPs was comparable to that by USPBs (Fig. S15–S18, ESI[†]). These above results demonstrated that CaPB NPs have a rapid and efficient ability to promote wound healing. Furthermore, to evaluate the effect of the CaPB NPs on wound healing from a histological point of view, Masson trichrome staining was performed on the regenerated skin tissues which were collected on day 13. Compared with the control group, the CaPB NP group presented a uniform and thick collagen bundle deposition, while the number of collagen fibers was less and non-uniform in the control group on day 13 post-treatment (Fig. 3e). In addition, more new hair follicles and new sebaceous glands were observed in the CaPB NP-treated group, all revealing that the successful regeneration of wound tissues was induced by CaPB NPs through promoting collagen deposition and hair follicles regeneration.

Then, we explored the mechanism of promoting wound healing induced by CaPB NPs. It is well known that angiogenesis plays a key role in wound proliferation and remodeling by providing progenitor cells, oxygen and nutrients.²⁹ Enzyme-linked immunosorbent assay (ELISA) and immunofluorescence technologies were applied for monitoring the status of angiogenesis, respectively. It was found that the expression of VEGF was up-regulated in the CaPB NP-treated wound in comparison

with that in the control group, and the level in the CaPB NP-treated group was increased by 2 times compared with that in the control group (Fig. 3d). Consistently, the treatment with CaPB NPs led to the obvious enhancement in the fluorescence intensity while there was little fluorescence observed in the control group, indicating the up-regulated CD31 expression mediated by CaPB NPs (Fig. 3f). Furthermore, according to the quantitative findings, the relative coverage area of CD31 in the CaPB NP-treated group was 5.3 times larger than that in the untreated group, indicating the better pro-vascularization capability of the CaPB NPs (Fig. S19, ESI[†]). The results showed that the CaPB NPs could promote neovascularization in the wound site. Besides, to demonstrate the functions and roles of Ca in promoting vessel formation, we also performed immunohistochemical staining for CD31 expression in the free Ca²⁺-treated group (Fig. S20, ESI[†]). CD31 expression was significantly higher in the free Ca²⁺-treated group compared to the untreated group, indicating that angiogenesis was significantly better after the treatment of free Ca²⁺. Notably, the CaPB NP-treated group showed the highest CD31 expression, indicating that the superior accelerated wound healing effect induced by CaPB NPs may be attributed to the synergistic effect of the antioxidant properties and the angiogenesis effect of Ca²⁺.

In addition to angiogenesis, we investigated the mechanism of promoting wound healing from the perspective of remodeling the wound microenvironment using hematoxylin and eosin

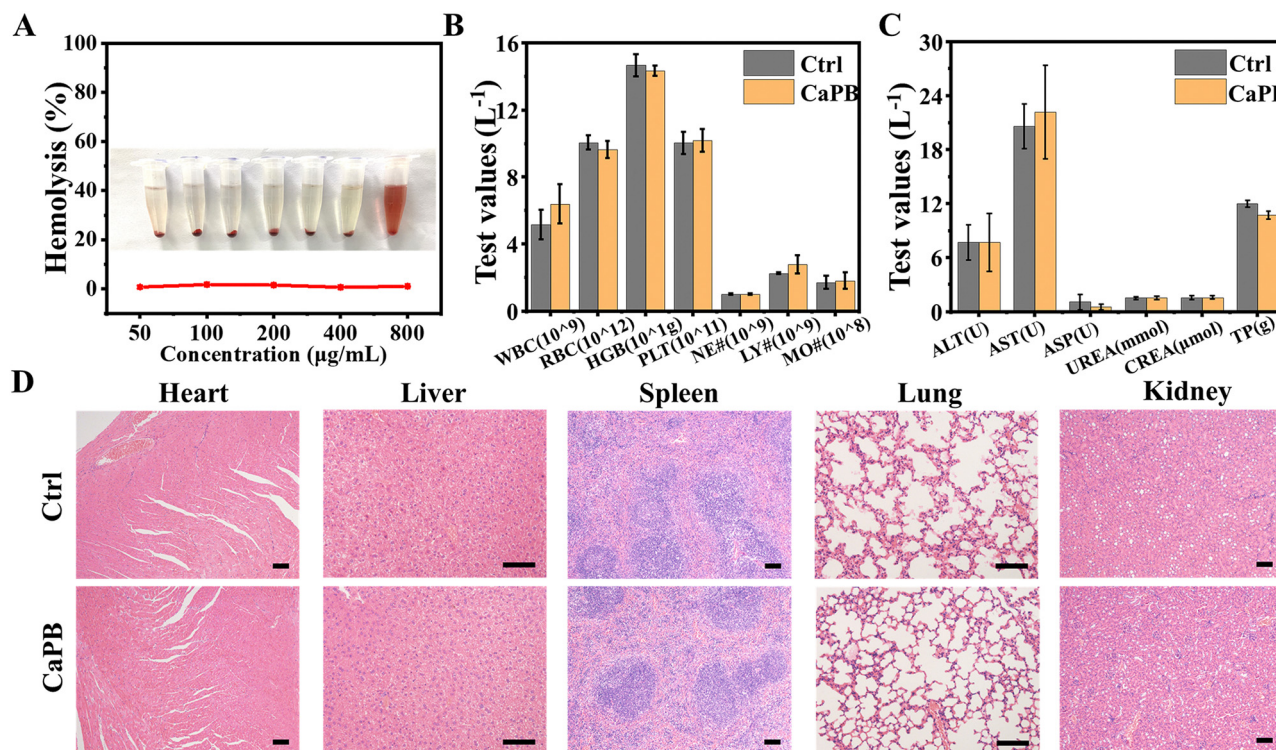


Fig. 4 Biosafety evaluation of CaPB NPs *in vivo*. (a) The percentage of the hemolysis rate of CaPB NPs with different concentrations. (b) Blood routine analysis of healthy mice after treatment with CaPB NPs. ($n = 3$, data are shown as mean \pm SD). (c) Serum analysis of healthy mice after treatment with CaPB NPs. ($n = 3$, data are shown as mean \pm SD). (d) H&E staining of main organs including heart, liver, spleen, lung and kidney in mice treated with CaPB NPs. The scale bar represents 100 μ m.

staining and ELISA technology. As shown in Fig. 3e, the wound tissue slices of the CaPB NP-treated group had less inflammatory cell infiltration, and the epithelial tissue was thinner and relatively intact, while the wound slices of the control group still had incomplete healing residual scabs, thicker epithelial tissues and unclear boundaries. Besides, ELISA results also showed that the treatment of CaPB NPs significantly promoted the expression of IL-4 and IL-10 compared with that in the untreated group on the 13th day (Fig. 3g and h), indicating that CaPB NPs could effectively promote the switch of macrophages from the pro-inflammatory phenotype to the anti-inflammatory phenotype. These above results suggest that the CaPB NPs up-regulated the expression anti-inflammatory factors in the wound site and promoted angiogenesis, thus accelerating tissue regeneration.

Biocompatibility of CaPB NPs *in vivo*

For biomedical applications, the biosafety of nanozymes is another key criterion. Therefore, a series of experiments were conducted to evaluate the biosafety of CaPB NPs and USPBs (Fig. S21, ESI[†]). Apart from no obvious cytotoxicity (Fig. S11 and S12, ESI[†]), the CaPB NPs did not induce hemolysis even up to 800 $\mu\text{g mL}^{-1}$ (Fig. 4a). Next, hematological and pathological examinations on mice were conducted to determine whether CaPB NPs cause toxicity *in vivo*. The blood routine (Fig. 4b) and biochemical (Fig. 4c) analyses showed that there was no appreciable difference in these indicators. Meanwhile, H&E staining images of the major organs of the CaPB NP-treated mice (liver, heart, spleen, lungs, and kidneys) showed no obvious difference in comparison with the untreated mice (Fig. 4d). Overall, these above results suggest that the CaPB NPs had excellent biocompatibility *in vitro* and *in vivo*.

Conclusions

In summary, we designed and synthesized Ca-doped Prussian blue nanoparticles by a simple polymer-mediated method. The induction of Ca into the structure enabled the realization of controllable size and mass production of PB NPs and meanwhile, the CaPB NPs exhibited CAT-like and SOD-like activities comparable to those of USPBs. Owing to the prominent ROS-scavenging activities, CaPB NPs effectively rescued cell viability upon oxidative stress *in vitro*. Furthermore, the *in vivo* treatment of CaPB NPs in the wound model mice showed that CaPB NPs exerted multiple bioactivities including antioxidant activity, modulating the inflammatory microenvironment, promoting collagen deposition and angiogenesis to achieve accelerated and complete wound healing. Overall, both excellent wound healing performance and their high biosafety endow CaPB NPs with high potential for clinical translation.

Experimental

Materials

Calcium chloride dihydrate ($\text{CaCl}_2 \cdot 2\text{H}_2\text{O}$, 99%) and potassium ferricyanide ($\text{K}_3[\text{Fe}(\text{CN})_6]$, 99.5%) were purchased from Aladdin

(Shanghai, China). Poly(vinylpyrrolidone) (PVP, K30) was purchased from J&K Chemical Technology (Beijing, China). Hydrochloric acid (HCl) and ethanol were acquired from Sinopharm Chemical Reagent Co. (Shanghai, China). Phosphate buffer solution (PBS) was purchased from Sangon Biotech (Shanghai, China). All chemicals were used without further treatment.

Synthesis and characterization of CaPB NPs

$\text{K}_3[\text{Fe}(\text{CN})_6]$ (10 mM) was dissolved in 20 mL of ultrapure water (solution A, $\text{pH} \approx 1$). CaCl_2 (10 mM) and PVP K30 (500 mg) were dissolved in another 20 mL ultrapure water (solution B, $\text{pH} \approx 1$). Following this, solution A was dropped into solution B while being stirred magnetically at ambient temperature. After stirring for further 10 min, the solution was added to a dialysis bag (molecular weight cut off (MWCO) $\approx 12\,000$) and stirred for 6 h. Finally, it was dried overnight under lyophilization. A transmission electron microscope (TEM, Tecnai G2 spirit BioTwin, FEI, USA) was used to analyze the morphology of the nanozyme as it had been created. Using a Talos F200X microscope (FEI, USA), energy-dispersive X-ray spectroscopy (EDX) elemental mapping was carried out. The crystallinity of the nanozyme was characterized by powder X-ray diffraction (PXRD) using a Bruker D8 Advance diffractometer equipped with $\text{Ca K}\alpha$ radiation ($\lambda = 1.5406 \text{ \AA}$). The X-ray photoelectron spectroscopy (XPS) analyses were carried out using an X-ray photoelectron spectroscope (ESCALAB 250XI, Thermo Fisher Scientific, USA) using a monochromatic $\text{Al K}\alpha$ X-Ray source (1486.6 eV). Inductively coupled plasma optical emission spectroscopy (ICP-OES, ICAP7200, Thermo Fisher, Germany) was used to measure the metal element concentrations of the nanozymes as they were manufactured. A Vertex 70 spectrometer from Bruker in Germany was used to measure the FT-IR spectra. Measurements of UV-vis absorption were performed.

Detection of the antioxidant properties of CaPB NPs and USPBs

The catalase assay kit (S0051, Beyotime, China) was used to measure the residual H_2O_2 in order to determine the CAT-like activity of CaPB NPs and USPBs. The reaction between H_2O_2 and ammonium molybdate produced a yellow complex with a characteristic absorption peak at 560 nm, which could be detected using a microplate reader (BioTek, USA). Various H_2O_2 concentrations (100, 200, 400, 600, 800, and 1000 μM) were added for the kinetic tests of nanozymes using H_2O_2 as the substrate.

The SOD-like activity of CaPB NPs and USPBs was measured by the ESR technique. In detail, BMPO was used as the spin trap to capture superoxide in the form of the spin adduct $\text{BMPO} \cdot \text{OOH}$ and the xanthine/XOD system was employed for the generation of $\text{O}_2^{\cdot -}$. The samples contained 1 mM BMPO, CaPB NPs and USPBs of various concentrations, 0.1 U mL^{-1} XOD, 0.05 mM DTPA and 1 mM xanthine. Samples were placed in quartz capillary tubes and then the ESR spectra were measured after 5 min. The condition for ESR measurements in the detection of the spin adducts $\text{BMPO} \cdot \text{OOH}$: 2 mW microwave power; 80 G scan range and 1 G field modulation.

CaPB NPs and USPBs protect cells from oxidative damages

The HUVEC cells were incubated in the 96-well cell culture cluster for 24 h with the cell density at 60–80%; then, the medium of cells was replaced by the fresh medium containing H₂O₂ (1 mM) for 2 h. Then, the cells were treated with CaPB NPs and USPBs separately for 4 h. The treated cells were cultured in a constant temperature incubator at 37 °C and 5% CO₂. Following the aforementioned treatments, the cell viability was detected using the CCK-8 viability test kit. Finally, the microplate reader (BioTek, USA) was used to assess the vitality of the cells.

In vivo wound healing experiments

All animal experiments were approved by the Ethical Committee of Soochow University. The chronic wound healing experiments were conducted on male Balb/c mice (20–22 g). The mice's backs were first shaved and cleaned with 75% ethanol. Then, a scissor was used to create a full-thickness wound (diameter: 10 mm) on the mice's backs. Following a 24 hour period, the infected mice were separated into three groups ($n = 3$) and given PBS (50 μ L), CaPB NPs (50 μ L, 400 μ g mL⁻¹), CaCl₂ (50 μ L, 10 μ g mL⁻¹), or USPBs (50 μ L, 400 μ g mL⁻¹), respectively. Every three days, the wound sites were measured using a digital caliper and photographed. The following equation was used to determine the wound healing rates:

Wound healing rate

$$= \frac{\text{Wound area (day 0)} - \text{Wound area (day } n\text{)}}{\text{Wound area (day 0)}} \times 100\%$$

Histology and immunohistochemistry, inflammation associated cytokine expression and immunofluorescence staining

The wound tissues from mice were excised and collected after 13 days post-treatment which were prepared for Masson's trichrome and H&E staining and immunofluorescence staining of CD31 (ab281583, Abcam, China). The wound tissues harvested on day 13 were also utilized to measure the levels of the inflammatory factors IL-4 (70-EK283/2-96, Lianke Bio, China), IL-10 (70-EK204/2-96, Lianke Bio, China) and the angiogenesis proteins VEGF (70-EK210/2-96, Lianke Bio, China). The protein concentration of the wound tissue was measured using the Enhanced BCA Protein Assay Kit (P0010, Beyotime, China). In addition, the major organs, including the heart, liver, spleen, kidneys and lungs, were harvested and stained with HE on day 13.

Author contributions

Qingrong Dong: methodology, data curation and writing – original draft. Ge Fang: conceptualization, data curation, writing – original draft, funding acquisition and editing. Fang Liu: methodology and investigation. Shuwei Cai: writing – review. Yujie Tao: writing – review. Tingyu Xue: methodology and validation. Minghua Tang:

investigation and validation. Kun Zhang: investigation and data curation. Ziheng An: software. Jiangfeng Du: conceptualization, project administration, funding acquisition and editing. Hui Zhang: conceptualization, project administration, funding acquisition, and writing – review and editing.

Conflicts of interest

There are no conflicts to declare.

Acknowledgements

This work was financially supported by the National Natural Science Foundation of China (No. U21A20386, No. 31901000 and No. 81901889), the Postdoctoral Science Foundation of Jiangsu Province (No. 2019K152) and the Collaborative Innovation Center of Radiological Medicine of Jiangsu Higher Education Institutions.

Notes and references

- 1 V. Falanga, R. R. Isseroff, A. M. Soulika, M. Romanelli, D. Margolis, S. Kapp, M. Granick and K. Harding, *Nat. Rev. Dis. Primers*, 2022, **8**, 50.
- 2 R. G. Frykberg and J. Banks, *Adv. Wound Care*, 2015, **4**, 560–582.
- 3 A. J. M. Boulton, L. Vileikyte, G. Ragnarson-Tennvall and J. Apelqvist, *Lancet*, 2005, **366**, 1719–1724.
- 4 S. A. Eming, T. A. Wynn and P. Martin, *Science*, 2017, **356**, 1026–1030.
- 5 G. Morris, M. Gevezova, V. Sarafian and M. Maes, *Cell Mol. Immunol.*, 2022, **19**, 1079–1101.
- 6 H. Kim, S. Y. Wang, G. Kwak, Y. Yang, I. C. Kwon and S. H. Kim, *Adv. Sci.*, 2019, **6**, 1900513.
- 7 D. Xu, L. Wu, H. Yao and L. Zhao, *Small*, 2022, **18**, 2203400.
- 8 M.-J. Kwon, B. Kim, Y. S. Lee and T.-Y. Kim, *J. Dermatol. Sci.*, 2012, **67**, 81–87.
- 9 Y. Zhu, Y. Matsumura, M. Velayutham, L. M. Foley, T. K. Hitchens and W. R. Wagner, *Biomaterials*, 2018, **177**, 98–112.
- 10 A. Larranaga, I. L. M. Isa, V. Patil, S. Thamboo, M. Lomora, M. A. Fernandez-Yague, J. R. Sarasua, C. G. Palivan and A. Pandit, *Acta Biomater.*, 2018, **67**, 21–31.
- 11 G. D. Krischak, P. Augat, L. Claes, L. Kinzl and A. Beck, *J. Wound Care*, 2007, **16**, 76–78.
- 12 Y. Huang, J. Ren and X. Qu, *Chem. Rev.*, 2019, **119**, 4357–4412.
- 13 D. Jiang, D. Ni, Z. T. Rosenkrans, P. Huang, X. Yan and W. Cai, *Chem. Soc. Rev.*, 2019, **48**, 3683–3704.
- 14 L. Valgimigli, A. Baschieri and R. Amorati, *J. Mater. Chem. B*, 2018, **6**, 2036–2051.
- 15 H. Sun, Y. Zhou, J. Ren and X. Qu, *Angew. Chem., Int. Ed.*, 2018, **57**, 9224–9237.
- 16 Z. Qin, Y. Li and N. Gu, *Adv. Healthcare Mater.*, 2018, **7**, 1800347.

- 17 M. Shukla, N. V. Verma, Z. Mohanta, S. Tripathi and A. Pandya, *Coord. Chem. Rev.*, 2023, **496**, 215414.
- 18 Z. Qin, Y. Li and N. Gu, *Adv. Healthcare Mater.*, 2018, **7**, e1800347.
- 19 J. Li, X. Liu, L. Tan, Z. Cui, X. Yang, Y. Liang, Z. Li, S. Zhu, Y. Zheng, K. W. K. Yeung, X. Wang and S. Wu, *Nat. Commun.*, 2019, **10**, 4490.
- 20 A. Sahu, J. Jeon, M. S. Lee, H. S. Yang and G. Tae, *Mater. Sci. Eng., C*, 2021, **119**, 111596.
- 21 M. Li, X. Li, Y. Gao, Y. Yang, C. Yi, W. Huang, B. Shen, D. Qi, Z. Mao and J. Wu, *Int. J. Biol. Macromol.*, 2023, **242**, 125144.
- 22 H. Ming, N. L. K. Torad, Y.-D. Chiang, K. C. W. Wu and Y. Yamauchi, *CrystrEngComm*, 2012, **14**.
- 23 Z. Qin, B. Chen, Y. Mao, C. Shi, Y. Li, X. Huang, F. Yang and N. Gu, *ACS Appl. Mater. Interfaces*, 2020, **12**, 57382–57390.
- 24 H. Wang, Y. Shen, L. Chen, K. Li, Y. Shi, Z. Xu, D. Li, H. Chen, W. Wang and L. Gao, *Mater. Today Nano*, 2023, **22**, 100326.
- 25 S. Restrepo and K. Basler, *Nat. Commun.*, 2016, **7**, 12450.
- 26 A. Celli, C. L. Tu, E. Lee, D. D. Bikle and T. M. Mauro, *J. Invest. Dermatol.*, 2021, **141**, 2577–2586.
- 27 K. Wang, Y. Zhang, W. Mao, W. Feng, S. Lu, J. Wan, X. Song, Y. Chen and B. Peng, *Adv. Funct. Mater.*, 2021, **32**, 2109221.
- 28 M. Xu, H. Gao, Q. Ji, B. Chi, L. He, Q. Song, Z. Xu, L. Li and J. Wang, *J. Colloid Interface Sci.*, 2022, **609**, 364–374.
- 29 C. Xing, H. Zhu, X. Dou, L. Gao, S. Baddi, Y. Zou, C. Zhao, Y. Peng, Y. Fang and C. L. Feng, *ACS Nano*, 2023, **17**, 6275–6291.